Core to ultracompact HII region evolution in the W49A massive protocluster

T. Nony, R. Galván-Madrid, N. Brouillet, G. Suárez, F. Louvet, C. G. de Pree, M. Juárez-Gama, A. Ginsburg, K. Immer, Y. Lin, et al.

A&A, 687, A84 (2024)
https://doi.org/10.1051/0004-6361/202449279

Astronomy & Astrophysics

Core to ultracompact HII region evolution in the W49A massive protocluster*

T. Nony[1,2], R. Galván-Madrid[2], N. Brouillet[3], G. Suárez[4], F. Louvet[5], C. G. De Pree[6], M. Juárez-Gama[7], A. Ginsburg[8], K. Immer[9], Y. Lin[10], H. B. Liu[11,12], C. G. Román-Zúñiga[13], and Q. Zhang[14]

[1] INAF - Osservatorio Astrofisico di Arcetri, Largo E. Fermi 5, 50125 Firenze, Italy
e-mail: thomas.nony@inaf.it
[2] Instituto de Radioastronomía y Astrofísica, Universidad Nacional Autónoma de México, Morelia, Michoacán 58089, Mexico
[3] Laboratoire d'astrophysique de Bordeaux, Univ. Bordeaux, CNRS, B18N, allée Geoffroy Saint-Hilaire, 33615 Pessac, France
[4] Department of Astrophysics, American Museum of Natural History, Central Park West at 79th Street, NY 10024, USA
[5] Univ. Grenoble Alpes, CNRS, IPAG, 38000 Grenoble, France
[6] National Radio Astronomy Observatory, 520 Edgemont Road, Charlottesville, VA 22903, USA
[7] Instituto Nacional de Astrofísica, Óptica y Electrónica, Luis E. Erro 1, 72840 Tonantzintla, Puebla, Mexico
[8] Department of Astronomy, University of Florida, PO Box 112055, USA
[9] Leiden Observatory, Leiden University, PO Box 9513, 2300 RA Leiden, The Netherlands
[10] Max-Planck-Institut für Extraterrestrische Physik, Giessenbachstr. 1, 85748 Garching bei München, Germany
[11] Department of Physics, National Sun Yat-Sen University, No. 70, Lien-Hai Road, Kaohsiung City 80424, Taiwan, R.O.C.
[12] Center of Astronomy and Gravitation, National Taiwan Normal University, Taipei 116, Taiwan
[13] Universidad Nacional Autónoma de México, Instituto de Astronomía, AP 106, Ensenada 22800, BC, Mexico
[14] Center for Astrophysics, Harvard & Smithsonian, 60 Garden St., Cambridge, MA 02420, USA

Received 19 January 2024 / Accepted 2 April 2024

ABSTRACT

Aims. We aim to identify and characterize cores in the high-mass protocluster W49A, determine their evolutionary stages, and measure the associated lifetimes.
Methods. We built a catalog of 129 cores extracted from an ALMA 1.3 mm continuum image at 0.26″ (2900 au) angular resolution. The association between cores and hypercompact or ultracompact HII (H/UC HII) regions was established from the analysis of VLA 3.3 cm continuum and H30α line observations. We also looked for emission of hot molecular cores (HMCs) using the methyl formate doublet at 218.29 GHz.
Results. We identified 40 cores associated with an H/UC HII region and 19 HMCs over the ALMA mosaic. The 52 cores with an H/UC HII region and/or an HMC are assumed to be high-mass protostellar cores, while the rest of the core population likely consists of prestellar cores and low-mass protostellar cores. We found a good agreement between the two tracers of ionized gas, with 23 common detections and only four cores detected at 3.3 cm and not in H30α. The spectral indexes from 3.3 cm to 1.3 mm range from 1, for the youngest cores with partially optically thick free-free emission, to about −0.1, which is for the optically thin free-free emission obtained for cores that are likely more evolved.
Conclusions. Using the H/UC HII regions as a reference, we found the statistical lifetimes of the HMC and massive protostellar phases in W49N to be about 6×10^4 yr and 1.4×10^5 yr, respectively. We also showed that HMCs can coexist with H/UC HII regions during a short fraction of the core lifetime, about 2×10^4 yr. This indicates a rapid dispersal of the inner molecule envelope once the HC HII is formed.

Key words. stars: formation – stars: protostars – ISM: clouds – HII regions – ISM: molecules

1. Introduction

The evolutionary sequence and timescales of the formation of high-mass stars are still poorly constrained (see e.g., the review by Motte et al. 2018), partly because of observational difficulties related to low-number statistics and large distances within the Milky Way. W49A is among the few molecular clouds that enable us to study, in a single region and with robust statistics, the various evolutionary stages of high-mass star formation, which are briefly descibed in the following paragraph. Young massive protostars first drive strong molecular outflows and heat the inner part of their envelope. Complex organic molecules (COMs) are released from the grains in the heated region (Herbst & van Dishoeck 2009), which is called the hot molecular core (HMC) and is thus characterized by multiple lines from COMs – the so-called line forest. In contrast to their low-mass analogs, high-mass protostars are still embedded in their nascent envelope when they evolve to the main sequence. The extreme ultraviolet (EUV) radiation from high-mass stars (>8 $M_\odot$) is sufficient to ionize hydrogen and create an HII region (Churchwell 2002). As the luminosity of the star keeps increasing, the HII region expands and breaks through the core and eventually impacts the whole molecular cloud. Hypercompact (HC) HII regions

* The reduced ALMA and VLA data of W49A used in this work are available at the CDS via anonymous ftp to cdsarc.cds.unistra.fr (130.79.128.5) or via https://cdsarc.cds.unistra.fr/viz-bin/cat/J/A+A/687/A84

Table 1. Parameters of the continuum images and spectral cubes.

Image	Instr.	ν_{obs} [a] [GHz]	Bandwidth [b] [MHz]	pixel [″]	Resolution [c] [″ × ″]	[km s^{-1}]	1σ rms [mJy beam^{-1}] [d]
X band cont.	VLA	9.107	688	0.06	0.29 × 0.24	–	0.22
Band 6 cont.	ALMA	227.950	1230	0.06	0.29 × 0.24	–	0.38
Spw 0	ALMA	217.900	1875	0.07	0.28 × 0.23	0.67	1.47
Spw 1	ALMA	219.860	1875	0.07	0.28 × 0.25	0.67	1.67
Spw 2/H30α	ALMA	231.870	1875	0.07	0.27 × 0.20	0.63	1.57
Spw 3	ALMA	233.740	1875	0.07	0.27 × 0.20	0.63	1.57

Notes. [a]Central frequency of the continuum images or of the spectral windows. The central frequency of the ALMA continuum image is computed as the intensity-weighted average frequency, with a spectral index of three (see Eq. (1) in Ginsburg et al. 2022). [b]Bandwidth used to create the continuum images or bandwidth of the cubes. [c]Beam FWHM and channel width. The data cubes have been produced using the default Hanning smoothing function without channel averaging ($N = 1$), resulting in a spectral resolution of two channels. [d]1 mJy beam^{-1} corresponds to 0.34 K at 230 GHz and to 222 K at 9 GHz for the continuum maps.

are usually interpreted as the youngest stage of ionization by a massive star (e.g., Keto 2007; Tanaka et al. 2016), confined within cores of sizes ∼10^{-2} pc or even less and having electron densities $n_e > 10^6$ cm^{-3} (Kurtz 2005). Ultracompact (UC) HII regions are by definition expected to be larger and less dense by at least one order of magnitude. However, deep centimeter surveys of protocluster regions (e.g., Ginsburg et al. 2016) have shown that the most common type of hypercompact-sized HII regions have lower densities, in the range of 10^4 to $<10^6$ cm^{-3} (Rivera-Soto et al. 2020). Since a reliable distinction between these two types of objects requires modeling of the centimeter to (sub)millimeter spectral energy distribution (e.g., Keto et al. 2008; Galván-Madrid et al. 2009; Zhang et al. 2022), we refer to all of our detections of small HII emission as H/UC HII regions.

Located at a distance of 11.1 kpc from the Sun (Zhang et al. 2013), W49A is one of the most luminous protoclusters in the Galaxy ($L \sim 2.6 \times 10^7\ L_\odot$, Sievers et al. 1991; Lin et al. 2016). The W49A giant molecular cloud (GMC) has been mapped from ∼100 pc to sub-parsec scales in the (sub)millimeter continuum and in molecular lines down to angular resolutions of a few arcseconds (e.g., Miyawaki et al. 2009; Peng et al. 2010; Galván-Madrid et al. 2013; Barnes et al. 2020). The W49A GMC can be divided into three subcomponents, labeled as W49 north (W49N), W49 south (W49S), and W49 southwest (W49SW). From CO observations, Galván-Madrid et al. (2013) evaluated the gas mass of the W49A GMC within a radius of 60 pc to be $10^6\ M_\odot$, with the main star-forming hub W49N concentrating $M_{gas} \sim 2 \times 10^5\ M_\odot$ within a radius of 6 pc. A cluster of massive stars with a total mass of about $10^4\ M_\odot$ has been identified in the near infrared by Homeier & Alves (2005) at about 3 pc east of the center of W49N. The study of Saral et al. (2015) with *Spitzer* also revealed 232 Class 0/I Young Stellar Objects in the entire W49A GMC. About 50 HC and UC HII regions have been detected in W49A (e.g., Welch et al. 1987; De Pree et al. 1997, 2020). The embedded and infrared-visible stellar populations already drive significant feedback across the GMC (Rugel et al. 2019). Prominent water maser features extending to hundreds of kilometers per second from the cloud velocity have been reported within W49N (e.g., Gwinn et al. 1992; McGrath et al. 2004). Also, five 6.7 GHz methanol masers were reported in the catalog of Breen et al. (2015). Finally, Wilner et al. (2001) reported the detection of six HMCs in W49N using CH_3CN observations at subarcsecond resolution, and Miyawaki et al. (2022b) studied the HMC W49N MCN-a (UCHII region J1 in De Pree et al. 1997).

The star-forming core population and star-formation sequence in W49A, however, have not been explored in detail so far. In this work, we present a subarcsecond resolution study of W49A aimed at identifying and characterizing its core populations as well as the evolutionary sequence from young star-forming cores to UCHII regions. The Atacama Large Millimeter/submillimeter Array (ALMA) and Very Large Array (VLA) observations we used are presented in Sect. 2. The analysis of the continuum maps and molecular lines presented in Sect. 3 is used in Sect. 4 to characterize the dust cores and establish a temporal classification based on their association with HMCs and UC HII regions. A discussion is proposed in Sects. 5 and 6 summarizes our main conclusion.

2. Observations

2.1. ALMA data

Observations of W49A at 1.3 mm (Band 6) were carried out with ALMA in Cycle 5 (project 2016.1.00620.S, PIs: Ginsburg, Galván-Madrid) between 2017 and 2018. The data consist of a mosaic of 28 fields with a primary beam of 25.6″, for a total mapping extent of about 2.5′ × 1.6′ (8.2 × 5.3 pc). The maximum recoverable scale of the 12-m array configuration used in this work is about 11″.

Continuum data were processed with `CASA` version 5.4 (CASA Team 2022) using the imaging and self-calibration pipeline developed by the ALMA-IMF consortium (described in detail in Ginsburg et al. 2022). The continuum map has been produced using a selection of line-free channels (equivalent to the `cleanest` maps in Ginsburg et al. 2022) from the four spectral windows (hereafter Spws) of the dataset, summing up to a bandwidth of 1.23 GHz. We performed three iterations of cleaning and phase self-calibration and one iteration of amplitude self-calibration using model masks of increasing size and decreasing cleaning thresholds. We used the multi-term (multi scale) multi-frequency synthesis deconvolver of `tclean` with two Taylor terms, a robust parameter of zero, and scales up to nine times larger than the synthesized beam. The final beam of the 1.3-mm continuum image has a full-width-half-maximum (FWHM) size of 0.29″ × 0.24″ (≈2900 au at 11.1 kpc). The rms noise measured in regions far away from the brightest emission, where the map is not limited by dynamic range, is of 0.38 mJy beam^{-1} (see Table 1).

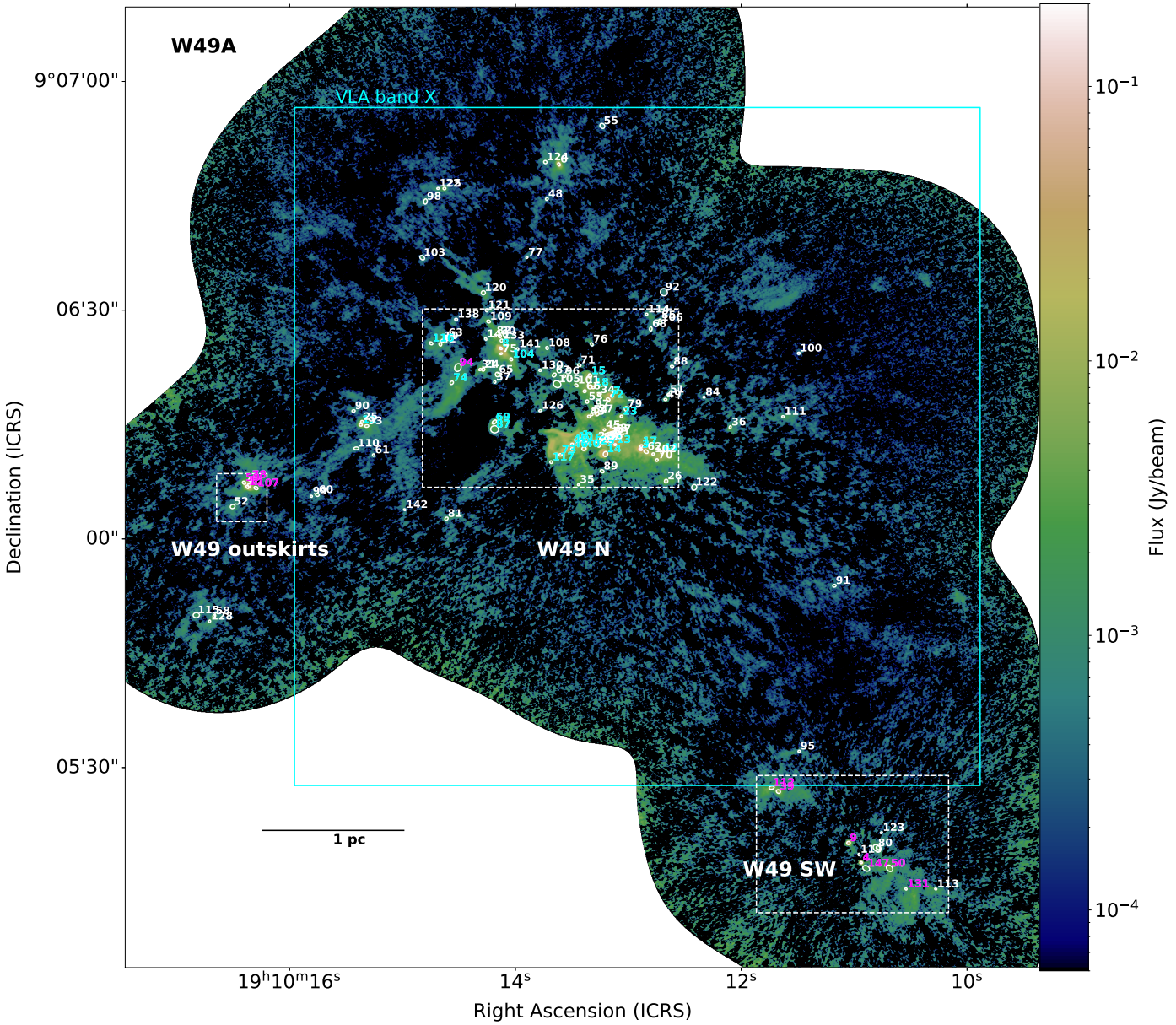

Fig. 1. The W49A protocluster as imaged at 1.3 mm using ALMA. Dust cores are represented by their FWHM ellipses in white and numbered in cyan for cores also detected at 3.3 cm. In magenta numbers are cores detected only in H30α, and in white numbers are non-detections at both 3.3 cm and H30α. The field of view of the VLA *X* band image is represented with a solid cyan line. A scale bar is shown. Zoom-ins of the three main regions of interest (W49N, W49SW and W49 outskirts) delimited by white dashed lines are shown in Figs. 2 and 3.

For the line data, the four spectral windows were processed with `IMAGER`[1], implemented within the `GILDAS` software[2]. Cleaning was performed using Clark deconvolution and 0.1 robust weighting. The cubes across the four bands have a spatial resolution of approximately 0.24″ (2750 au), a channel width of 0.65 km s^{-1}, and an rms noise of 1.6 mJy beam^{-1} (0.6 K) per channel. The detailed parameters for each spectral window are given in Table 1. We have used the method presented in Molet et al. (2019) and Brouillet et al. (2022) to separate the continuum and spectral line emission in each pixel of the image plane. The Spw 2 band covers the H30α line at 231.9 GHz. We also used the Spw 0 and Spw 3 bands to analyze CH_3OCHO lines.

[1] https://imager.oasu.u-bordeaux.fr
[2] http://www.iram.fr/IRAMFR/GILDAS

2.2. VLA data

We used the VLA A-array continuum image at 3.3 cm (*X* Band) presented in De Pree et al. (2020). This image was created with the purpose of only studying W49N. Its field of view is outlined in Fig. 1. We smoothed this image from its original angular resolution (0.16″) to the resolution of the B6 ALMA continuum image (0.26″), then corrected it for its primary-beam response and regridded it to the ALMA image frame.

Juárez-Gama et al. (in prep.) used this image to provide a dendrogram catalog of H/UC HII regions and their physical properties in W49N. Their catalog of 79 H/UC HIIs is consistent with, and more complete than, previous visual identifications of H/UC HIIs in this protocluster (e.g., De Pree et al. 2005, 2020). We used the centimeter continuum catalog of Juárez-Gama et al. to complement the identification of dust cores and

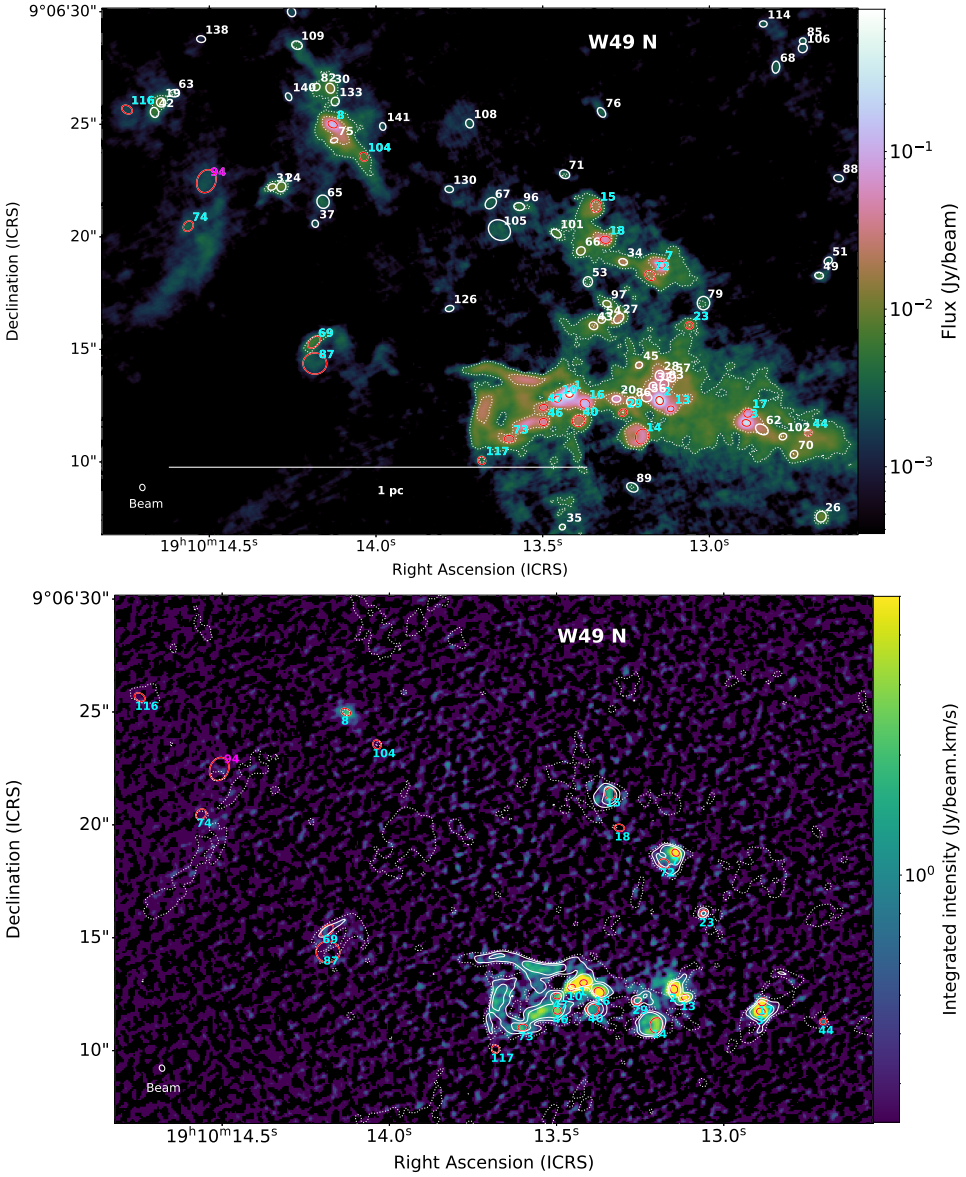

Fig. 2. Maps of the 1.3 millimeter continuum and recombination line toward W49N at the center of W49A. Top panel: ALMA B6 continuum image, contours are 10 and 40 sigma. Bottom panel: moment 0 map of H30α (color) and VLA X band map (contours). Contours are 3 sigma (dotted lines), 15, and 40 sigma (solid lines). Dust cores are represented by their FWHM ellipses and numbered with the same colors as in Fig. 1. Cores detected in the X band and/or in H30α are shown in red. The top panel also shows the remainder of the core catalog in white. Beams are shown in the lower-left corner. A scale bar is shown in the top panel.

HMCs reported in this paper as well as the HII emission traced by H30α also presented in this paper.

3. Analysis of the continuum maps and molecular lines

3.1. Core catalog

We used the `getsf` algorithm (Men'shchikov 2021) to extract sources from the 1.3-mm continuum images. The `getsf` algorithm decomposes the image into various spatial scales and separates compact sources from their background and filamentary structures. It is therefore well suited to finding cores in complex environments such as high-mass star-forming regions. `getsf` has been extensively used in ALMA studies of protocluster regions (e.g., Pouteau et al. 2022; Nony et al. 2023). We found 129 cores that pass the post-selection filters for robust detection and measurements recommended by Men'shchikov (2021): signal-to-noise for the background-subtracted peak larger than two, source size smaller than four times the FWHM beam size, and ellipticity smaller than two. Table A.1 lists the retrieved parameters of the identified cores: position, major and minor axis FWHM, and position angle.

We also used `getsf` to measure the peak intensity and integrated flux of the cores in the ALMA B6 ($S^{\rm peak}_{\rm B6}$, $S^{\rm int}_{\rm B6}$) and VLA X band ($S^{\rm peak}_{\rm BX}$, $S^{\rm int}_{\rm BX}$) maps. Cores are marked in the B6 continuum map in Fig. 1 and in the zoom-in shown in Figs. 2 and 3. Complementarily, we directly measured the maximum intensity of the cores in both the B6 and X band continuum maps, $F^{\rm max}$,[3] and we computed the integrated flux from the sum of the pixel intensities (I) within the core FWHM: $F^{\rm int} = c\,\Sigma I\,A_{\rm pix}/A_{\rm beam}$, where $A_{\rm pix}$ is the pixel area and $A_{\rm beam} = \pi\,\theta_{\rm min}\theta_{\rm maj}/(4\ln(2))$ is the beam area. We set the constant $c = 1/\ln(2)$ to account for the core extension beyond its FWHM. We used this second set of parameters for the calculations presented in Sect. 4.2, in which we compare a continuum map dominated by thermal dust emission (ALMA B6 at 230 GHz) with one dominated by free-free emission (VLA X band at 9 GHz).

[3] Contrary to the peak intensity in the X band, $S^{\rm peak}_{\rm BX}$, which is measured at the center of the ellipse defined in the B6 map, $F^{\rm max}_{\rm BX}$ is measured on the brightest pixel within the ellipse.

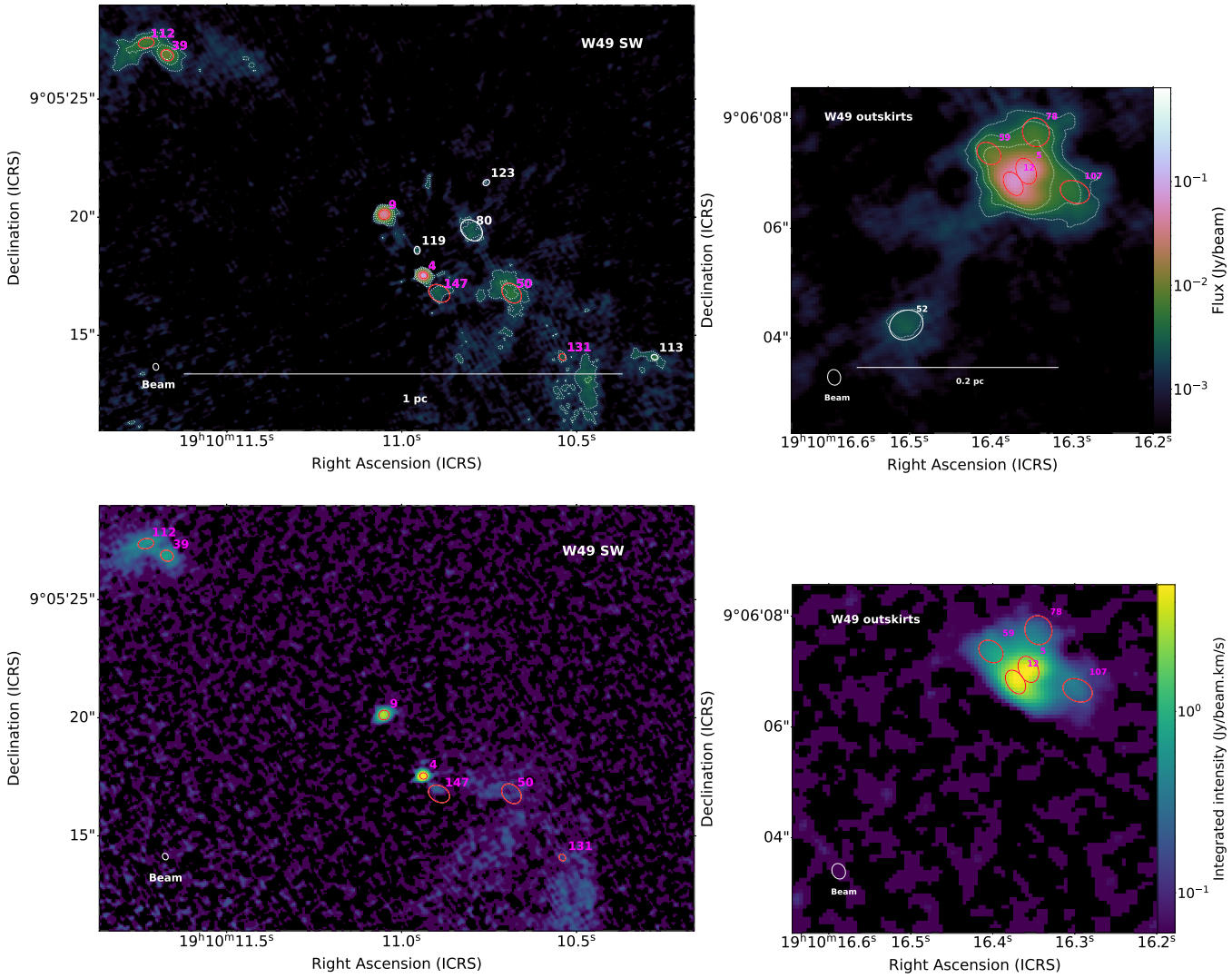

Fig. 3. Maps of 1.3 millimeter continuum and recombination line toward W49 SW (left panels) and the eastern outskirts (right panels). Top panel: Band 6 continuum image. Contours are 5, 10, and 20 sigma. Bottom panel: moment 0 map of H30α line. The same conventions of Fig. 2 apply for the ellipses and lines.

3.2. Recombination line and free-free emission

We identified cores associated with H/UC HII regions using two tracers of ionized gas, the H30α recombination line and the free-free emission measured using the *X* band map.

3.2.1. Detection of the H30α line

We identified cores associated with H30α emission using two complementary methods. Our first method is as follows. For all the cores, we inspected the spectrum at the frequency of the H30α line and performed Gaussian fitting to measure the line systemic velocity, the FWHM line width ΔV, and the peak brightness temperature $T_{\rm B}$. We then separated cores with a brightness temperature of $T_{\rm B}$ > 2 K (38 cores) from cores with $T_{\rm B}$ between 0.8 and 2 K (14'cores). There are $^{33}SO_2$ ($12_{3,9}$–$12_{2,10}$) lines very close in frequency (231.9004 GHz, 231.9015 GHz) to the H30α line at 231.9009 GHz as well as $CH_3C^{15}N$ and CH_3OCHO lines within 3 MHz. Therefore, disentangling the H30α emission can be challenging. Since the H30α line is expected to be much broader (see, e.g., the review of Hoare et al. 2007), we further applied a threshold for the linewidth of $\Delta V > 20$ km s^{-1} to filter out cores dominated by contamination from molecular lines. This gave us 29 cores with strong H30α detection ($T_{\rm B} > 2$ K) and nine with a weak detection.

Our second method relies on moment 0 maps of the H30α line, which we constructed by integrating in velocity from -50 km s^{-1} to $+50$ km s^{-1} (the line systemic velocity ranges from about 0 to 20 km s^{-1} LSR). We considered a positive detection when the core's FWHM ellipse includes a group of pixels above a given threshold. Considering the large dynamic range of the line emission in the map, we noticed that the noise strongly decreases from the center to the edges of the mosaic. In consequence, we defined two reference thresholds, $5\sigma_{\rm ctr} = 0.4$ Jy beam^{-1}km s^{-1} in the center and $5\sigma_{\rm sw} = 0.1$ Jy beam^{-1}km s^{-1} in the southwest region, and we constructed a clipped moment 0 map where pixels below 5σ are set to zeros. All of the 29 cores with a strong H30α line detection are also detected in the moment 0 maps and qualify as robust H30α detections. On the other hand, the nine cores with weak H30α line detection using the first method have a few isolated pixels above their respective threshold, at most, and we

considered them as tentative H30α detections. Cores with a robust or tentative H30α detection are overlaid on the moment 0 maps in the bottom panels of Figs. 2 and 3.

3.2.2. Detection of free-free centimeter emission

We defined the criterion for a robust detection and measurement in the X band as $S^{\rm peak}_{\rm BX} > 3\sigma_{\rm BX}$ and $F^{\rm max}_{\rm BX} > 3\sigma_{\rm BX}$, where $\sigma_{\rm BX} = 0.22\,{\rm mJy\,beam^{-1}}$ is the noise in the X band maps convolved to the B6 angular resolution, measured using the median absolute deviation. This criterion combines the background-subtracted peak intensity $S^{\rm peak}$ determined by *getsf* and the maximum intensity measured in the original continuum map (see Sect. 3.1). Out of the 109 cores lying in the field of view of the X band map, 27 have a robust detection at 3.3 cm. Table A.1 lists the integrated core fluxes in the X band ($F^{\rm int}_{\rm BX}$) and in Band 6 ($F^{\rm int}_{\rm B6}$).

3.3. Identification of hot molecular cores

We used methyl formate (CH_3OCHO) as a signature of HMC emission following the method described in Brouillet et al. (2022), where it was found that the use of methyl formate to identify the main HMCs in the W43-MM1 region provides similar results compared to the use of a broad frequency band with various other lines of complex organic molecules (see their Fig. 5). This study showed that this molecule offers a good compromise between widespread detectability and reliability in tracing HMCs. Methyl formate has also been used to identity HMC candidates in the recent survey of Bonfand et al. (2024). We based the identification on the CH_3OCHO ($17_{3,14}$–$16_{3,13}$) doublet at 218.281 and 218.298 GHz, with an upper-level energy $E_{\rm u}$ of 99.7 K. We further verified our detections with a synthetic spectrum fitting the numerous methyl formate lines in Spw 3. We found 19 dust cores with HMC emission within the entire ALMA mosaic: 17 within the field of view of the X band map and two in the southwestern region. These cores with HMC emission are indicated with an asterisk in Table A.1.

4. Characterization of dust cores

From the measurements presented in Sect. 3, we identify cores associated with H/UC HII regions in Sect. 4.1 and measure their properties in Sect. 4.2. The inclusion of HMCs enables us to refine the evolutionary status of cores in Sect. 4.3.

4.1. Classification of cores with H/UC H II regions

4.1.1. With VLA measurements

For 109 cores within the field of view of the X band image, we had information on both the X band and the H30α detection. The 27 cores with a robust detection in the X band are likely associated with an H/UC HII region. Twenty were also detected in H30α, and three had a tentative H30α detection (#74, #87, #116). The remaining four cores without detection in H30α (#8, #18, #104, #117) only had a weak X band detection, with $S^{\rm peak}_{\rm BX}$ and $F^{\rm max}_{\rm BX}$ between 3 and 10$\sigma_{\rm BX}$, which suggests that our sensitivity to detect ionized gas is higher in the X band map than with the recombination line. Two other cores had a tentative H30α detection and no detection in X band. After visual inspection, we considered one of them (core #94) to be an H/UC HII region candidate, and the other (core #82) was rejected.

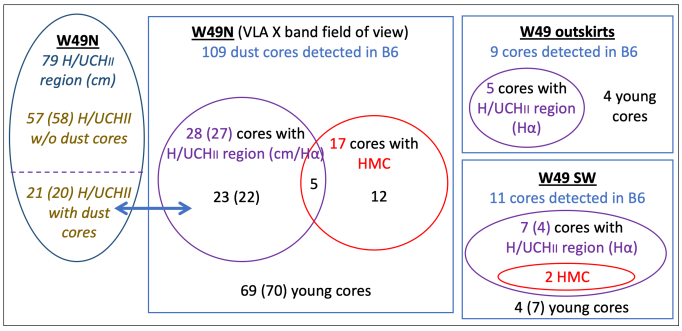

Fig. 4. Classification of the dust cores extracted in the ALMA Band 6 maps based on the detection of HMCs and/or HII region emission. Cores lying within the field of view of the VLA map (W49N) are separated from the cores in W49SW and in the eastern outskirts.

Our identification of dust cores associated with H/UC HII regions largely overlaps with the independent dendrogram catalog of H/UC HII regions of Juárez-Gama et al. (in prep.; see Sect. 2.2). Twenty-one H/UC HII dendrogram structures out of 79 within the X band map are associated with a core with an H/UC HII region, as previously defined. In detail, 20 HII dendrogram structures are associated with 26 cores with a robust detection in the X band[4]. Only one HII dendrogram structure is associated with a dust core (#27) not detected in the X band. Conversely, only one dust core with a detection in the X band is not associated with a dendrogram structure. This core (#18) is among the weakest X band detections ($S^{\rm peak}_{\rm BX} = 4\sigma_{\rm BX}$ and $F^{\rm max}_{\rm BX} = 3.4\sigma_{\rm BX}$) and is not found in H30α. Fifty-seven structures in the dendrogram catalog built from the X band map do not have any counterpart in the Band 6 core catalog and qualify as H/UC HII regions without association to dust cores. A summary of the relation between the 28 dust cores associated with H/UC HII regions (27 when excluding the H/UC HII region candidate) and the dendrogram-identified H/UC HII regions is shown in Fig. 4.

4.1.2. Without VLA measurements

For the 20 dust cores outside the field of view of the X band image, the recombination line is the only tool to search for emission from H/UC HII regions. Nine cores associated with a robust H30α detection (four in the southwestern region, five in the eastern outskirts; see Fig. 4) are likely associated with an H/UC HII region. After visual inspection, three additional cores with a tentative H30α detection located in the SW region (#50, #131, #147) were considered as H/UC HII region candidates, and another core located in the eastern outskirts (#115) was rejected.

4.2. Free-free emission in ALMA Band 6

Out of the 129 dust cores detected with ALMA over the entire mosaic, we found 36 cores associated with H/UC HII regions (27 with VLA measurements and 32 with H30α measurements; see Sect. 4.1) and four cores tentatively associated with H/UC HII regions (#50, #94, #131, #147), which have only tentative H30α detections. We used two methods to evaluate the free-free emission at 1.3 mm of these 40 cores associated with H/UC HII regions.

[4] Five dendrogram HII structures are associated with more than one dust core.

A first evaluation of the free emission was obtained from the integrated fluxes, $F^{\rm int}_{\rm BX}$, measured in the X band map over the FWHM of the cores (see Sect. 3.1):

$$F^{\rm int}_{\rm ff,cm} = F^{\rm int}_{\rm BX} \left(\frac{\nu_{\rm B6}}{\nu_{\rm BX}}\right)^{\alpha}, \quad (1)$$

where $\nu_{\rm B6}$ = 227.95 GHz and $\nu_{\rm BX}$ = 9.11 GHz are the reference frequencies of the ALMA B6 and VLA X band images, respectively (see Table 1). We took a spectral index of $\alpha = -0.1$, assuming that the free-free emission is optically thin all the way from 3 cm to 1 mm. The fluxes calculated in this way are thus lower limits to the free-free emission in the ALMA image.

We also constructed a pixel-by-pixel free-free map $I_{\rm ff,RL}$ using the moment 0 of the H30α recombination line (see, e.g., Wilson et al. 2009; Liu et al. 2019):

$$I_{\rm ff,RL} = 1.432 \times 10^{-4} (\nu_0^{-1.1} T_{\rm e}^{1.15})(1 + N_{\rm He}/N_{\rm H}) \int I_{\rm H30} {\rm d}v, \quad (2)$$

where the electron temperature is $T_{\rm e}$ = 7000 K (e.g., Zhang et al. 2023), the helium to hydrogen number ratio is $N_{\rm He}/N_{\rm H}$ = 0.08, and ν_0 is the central frequency of the H30α line. We then obtained a second evaluation of the free-free emission in B6 by measuring the integrated fluxes of the cores, $F^{\rm int}_{\rm ff,RL}$, on the $I_{\rm ff,RL}$ map using the method presented in Sect. 3.1.

From the previous measurements, we derived various parameters for the cores associated with the H/UC HII regions. The percentage of free-free emission in B6, defined as $P_{\rm ff} = F_{\rm ff,RL}/F_{\rm B6}$, ranges from 22 to 96%. The dust flux in B6 is expressed as $F_{\rm B6,dust} = F_{\rm B6} - F_{\rm ff}$, with $F_{\rm ff} = F_{\rm ff,RL}$ when the H30α is detected and $F_{\rm ff} = F_{\rm ff,cm}$ when otherwise. By construction, $F_{\rm ff,RL}$ can be expressed as a function of $F_{\rm B6,dust}$ and $P_{\rm ff}$: $F_{\rm ff,RL} = F_{\rm B6,dust} P_{\rm ff}/(1 - P_{\rm ff})$. We also computed the spectral index of free-free emission from $\nu_{\rm BX}$ to $\nu_{\rm B6}$:

$$\alpha_{\rm ff} = \frac{\log(F_{\rm ff,RL}/F_{\rm BX})}{\log(\nu_{\rm B6}/\nu_{\rm BX}).} \quad (3)$$

Finally, we computed the emission measure (EM) of the H/UC HII emission within dust cores:

$${\rm EM\ [pc\,cm^{-6}]} = \int n_e^2 {\rm d}l = 12\,\tau_{\rm ff} \left[\frac{\nu_{\rm BX}}{\rm GHz}\right]^{2.1} \left[\frac{T_{\rm e}}{\rm K}\right]^{1.35}, \quad (4)$$

with $n_{\rm e}$ as the electron density and $\tau_{\rm ff}$ as the free-free continuum optical depth, expressed as

$$\tau_{\rm ff} = -\ln\left[\left(1 - \frac{T_{\rm B}}{T_{\rm e}}\right)\right]. \quad (5)$$

The brightness temperature $T_{\rm B}$ was calculated from the maximum intensity in the X band within the FWHM of the cores, $F^{\rm max}_{\rm BX}$, and we used a constant electron temperature of $T_{\rm e}$ = 7000 K. Two cores with $T_{\rm B} > 7000$ K (#3 and #16) and four cores with $6700 < T_{\rm B} < 7000$ K (#1, #2, #7 and #14) are likely to have a higher electron temperature, considering the condition $T_{\rm e} > T_{\rm B}$ set by Eq. (5). We computed for these six cores a lower limit of the emission measure using an opacity of $\tau_{\rm ff}$ = 1.5, which is in line with the rest of the core sample. The emission measures of cores with H/UC HII regions range from 4.5×10^6 to 3.1×10^8 pc cm^{-6}, which are in the range of values found for ultra-compact HII regions (Churchwell 2002; Hoare et al. 2007). Table 2 lists the $F_{\rm ff,cm}$, $F_{\rm ff,RL}$, $P_{\rm ff}$, $\alpha_{\rm ff}$, and EM for the 40 cores with robust and candidate H/UC HII emission.

Table 2. Derived parameters of dust cores associated with H/UC HII regions.

n	$F^{\rm int}_{\rm ff,cm}$ [mJy.b^{-1}]	$F^{\rm int}_{\rm ff,RL}$ [mJy.b^{-1}]	$P_{\rm ff}$ [%]	α	EM [pc cm^{-6}]
1	26.3	809.1	>78	>0.96	>2.9e8
2	27.6	422.5	>58	>0.74	>2.9e8
3	40.3	224.2	>61	>0.43	>2.9e8
4	–	90.4	96	–	–
5	–	71.5	54	–	–
7	29.2	115.3	>61	>0.32	>2.9e8
8	1.1	–	–	–	1.1e7
9	–	55.8	65	–	–
10	8.8	179.6	54	0.83	1.8e8
11	15.8	24.6	44	0.04	1.4e8
12	–	65.3	56	–	–
13	9.2	94.8	64	0.62	1.1e8
14	97.1	137.1	>67	>0.00	>2.9e8
15	43.2	39.5	67	-0.13	1.9e8
16	49.6	176.5	63	0.29	2.9e8
17	12.7	80.5	64	0.47	1.7e8
18	0.7	–	–	–	4.5e6
23	9.1	11.0	62	-0.04	8.3e7
29	12.4	17.6	75	0.01	9.5e7
39	–	17.9	59	–	–
40	39.4	40.5	51	–0.09	1.5e8
44	1.0	8.1	37	0.53	8.7e6
46	24.9	35.3	61	0.00	3.1e8
47	14.6	23.7	54	0.05	1.6e8
50	–	9.1	25	–	–
59	–	11.2	49	–	–
69	12.4	13.6	64	–0.07	4.2e7
72	22.4	19.1	45	–0.15	1.1e8
73	21.6	25.0	55	–0.06	1.7e8
74	2.6	2.9	33	–0.07	1.4e7
78	–	8.1	37	–	–
87	10.0	13.7	42	–0.01	1.3e7
94	–	13.8	54	–	–
104	0.5	–	–	–	9.1e6
107	–	7.1	48	–	–
112	–	16.7	65	–	–
116	2.4	3.6	73	0.02	9.9e6
117	1.7	–	–	–	1.3e7
131	–	1.3	40	–	–
147	–	4.4	22	–	–

Notes. The table shows the core identifier, the integrated free-free flux at 1.3 mm estimated from the 3.3-cm map and from the H30α line, the percentage of free-free emission in Band 6, the spectral index of free-free emission, and the emission measure.

4.3. Core classification

We combined the statistics obtained from the detection rates of H/UC HII regions (see Sect. 4.1) with the HMC detections (see Sect. 3.3) to build a classification of the dust cores composed of four types: (a) cores without either an HMC or an H/UC HII region; (b) cores associated with an HMC but without an H/UC HII emission; (c) cores associated with both an HMC and H/UC HII emission; and (d) cores associated with an H/UC HII region but without an HMC emission. Within the full ALMA B6 mosaic, the number counts of each type are as follows: a): 77 (81), b): 12, c): 7, and d): 33 (29). The numbers

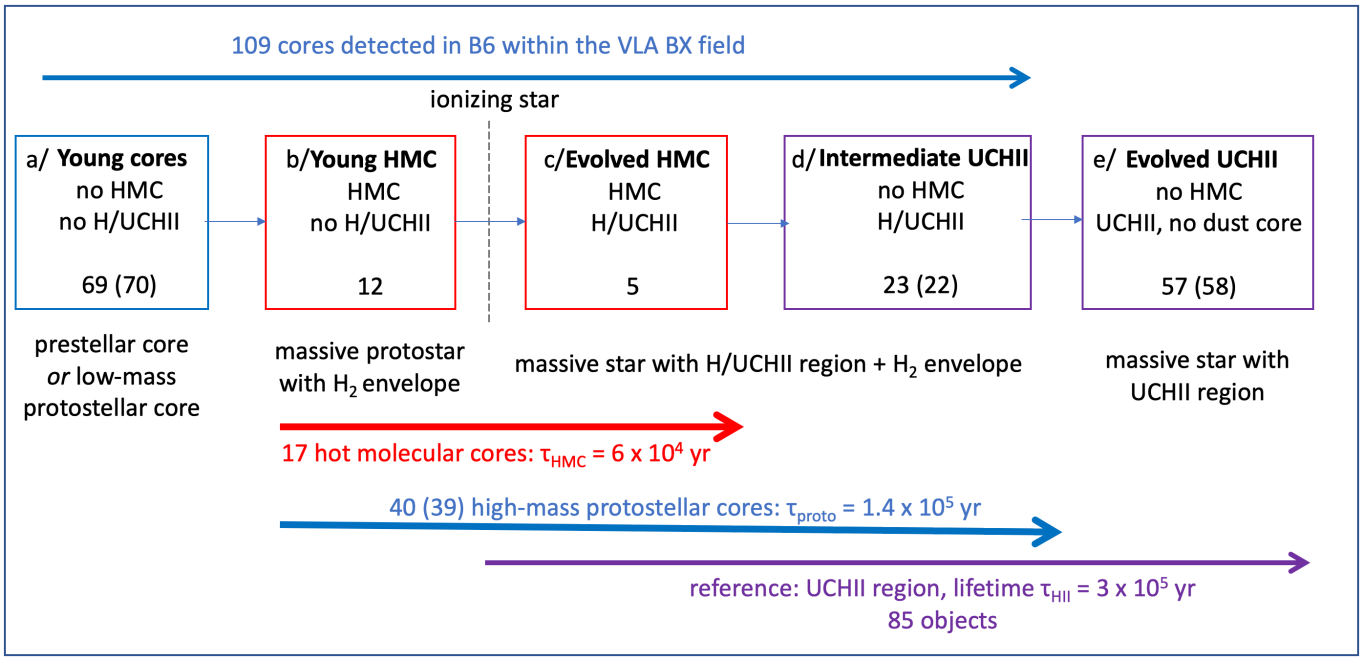

Fig. 5. Evolutionary sequence established for the cores extracted from the ALMA B6 maps within the *X* band field of view (W49N) based on the presence or absence of HMCs and H/UC HII regions. Statistical lifetimes for the various evolutionary stages were computed assuming a lifetime of the H/UC HII stage of 3×10^5 yr (see Sect. 5.3).

in parentheses correspond to the situation where all the cores with H/UC HII region candidates are accounted for in the first type. Within the smaller field of view of the VLA *X* band map, the statistics are 69 (70), 12, 5, and 23 (22). In Fig. 4, we show a diagram summarizing the detection statistics. In addition, 57 (58) H/UC HII regions without cores have been detected by Juárez-Gama et al. (in prep.).

5. Discussion

5.1. Evolution of star-forming cores in W49A

From the empirical classification presented in Sect. 4.3, in this section we propose an evolutionary sequence for the dust cores in W49A based on the presence or absence of the analyzed indicators of high-mass star formation. In Fig. 5, we summarize the proposed evolutionary scheme.

The cores in stage *a* do not show evidence of an HMC or H/UC HII region, and they are likely prestellar or low-mass protostellar cores. Among the cores in stage *a*, which we label "young cores", only a fraction are precursors of high-mass stars. It is indeed expected that some of them will produce low-mass objects. From stage *b* onward, all the cores are expected to harbor a high-mass ($\gtrsim$8 $M_\odot$) protostar. As it grows in mass, the protostellar object will first reach the luminosity necessary to heat its envelope to a temperature where complex organic molecules are released from dust grains. This defines the onset of the HMC (stage *b*: "young HMC" in Sect. 5). Later on when the EUV radiation of the star is sufficient to ionize atomic hydrogen, an HII region is born. During the short phase in which the HMC and the H/UC HII region coexist (stage *c*: "evolved HMC"), we expect that the remaining dust and molecules form a cocoon around the HII region, which is mostly free of dust (Lizano 2008). The radiation then becomes strong enough to fully destroy molecules, and only some dust remains around the H/UC HII region (stage *d*: "intermediate UCHII"). Finally, the UCHII fully clears its way out of the now extinct core, which is not detected anymore in dust emission (stage e: "evolved UCHII"). We expect that high-mass protostars keep accreting from their envelopes from stages b to d, which therefore represent the phases of high-mass protostellar evolution. Under this definition, 40 (39) cores out of 109 in W49N are high-mass protostellar cores. For W49SW and what we label as outskirts, 12 (9) cores out of 20 contain high-mass protostars (see Fig. 4).

Regarding their spatial distribution, a majority of the cores detected at 1.3 mm (109 out of 129) lie within the central star-forming region W49N. Only a few cores are located at distances beyond a parsec from the central hub (see Fig. 1). In W49N, HMCs and the well-known HII regions (De Pree et al. 1997, 2018) coexist with a population of young cores (see zoom-in Fig. 2). This indicates that the central protocluster is still actively forming stars in spite of the significant stellar feedback, as suggested by Galván-Madrid et al. (2013) from the measurement of a $\sim 2 \times 10^5$ $M_\odot$ molecular gas reservoir in W49N. A similar scenario has also been proposed for the very active W51-E and W51-IRS2 protoclusters (Ginsburg et al. 2016).

Using the uncertainties from the binomial distribution, we measured the 75% confidence interval for the percentage of cores containing high-mass protostars (stages b to d) to be 30–42% in W49N and 30–75% in W49SW and the W49 outskirts. Therefore, the relative abundance of high-mass protostars does not appear to be statistically different between the center of W49A and its periphery. We reached the same conclusion when considering only HMCs or cores with H/UC HII regions. This suggests that the different sub-protoclusters analyzed in this paper have a similar "age", in the sense that their core and protostellar populations look statistically similar. The small number of objects in W49SW and the W49 outskirts prevent us from making a stronger statement, but this further suggests that star formation across the W49A cloud started simultaneously, possibly by cloud-cloud collision, as suggested by Miyawaki et al. (2022a).

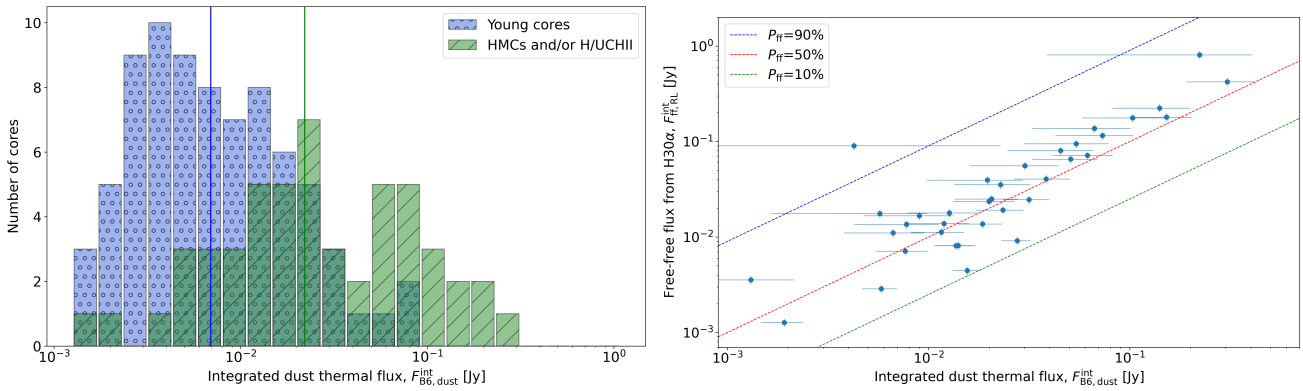

Fig. 6. Distribution of the core-integrated dust fluxes shown with a histogram (left) and compared to the distrubution of free-free fluxes (right). Left: cores with an HMC emission and/or an H/UC HII region (stages b to d, shown in green) are compared to the "young cores" without evidence of massive star formation (stage a, shown in blue). The vertical lines represent the median value of the distributions. Right: the core sample in this plot is made of the 35 cores with (robust or tentative) H30α detection, classified as cores with an H/UC HII region. The dashed lines represent constant values of the percentage of free-free emission $P_{\rm ff}$ with respect to the total core flux. Uncertainties were evaluated as 10% of the free-free and B6 fluxes.

5.2. Ionization evolution within dust cores

The physical parameters derived in Sect. 4.2 allowed us to evaluate the evolution of the protostar and envelope masses. The left panel of Fig. 6 shows that cores with an HMC and/or H/UC HII region have statistically higher dust flux than the others. The median dust flux of the two distributions are 2.2×10^{-2} Jy and 6.9×10^{-3} Jy, respectively. We verified with a KS test that the distributions are statistically distinct (p-value of 4×10^{-7}). Since the dust flux is related to the molecular gas mass of the core, this difference suggests that the more evolved cores could also be more massive. Complementarily, the right panel of Fig. 6 shows a strong correlation between the dust flux at 1.3 mm and the amount of free-free emission. Both the Pearson and Spearman correlation coefficients are higher than 0.8, with p-values $\simeq 10^{-10}$. Since the amount of free-free emission is related to the mass of the central star through the number of ionizing photons (e.g., Kurtz et al. 1994), this correlation could indicate that the mass of the central (proto)star grows simultaneously with the mass of its gas envelope. This hypothesis is in line with models of continuous accretion across multiple scales (e.g., Smith et al. 2009; Vázquez-Semadeni et al. 2019) as well as with recent observations suggesting that cores grow in mass as they evolve from quiescent (candidate prestellar) to active protostellar stages (Nony et al. 2023).

However, the dust flux is also dependent on the dust temperature, which might be higher in the more evolved cores than in the younger ones. This could partially explain the difference between the distributions in the left panel of Fig. 6. For an envelope internally heated by an embedded protostar, the dust temperature depends on its luminosity (Scoville & Kwan 1976) and hence on the protostellar mass. Therefore, the correlation found in the right panel of Fig. 6 between the dust and free-free fluxes could alternatively be explained by the dependence on the stellar mass of both quantities. Detailed measurements of core temperatures, which are beyond the scope of this work, are thus needed to draw firmer conclusions.

In Fig. 7 we compare the percentage of free-free emission in the 1.3 mm flux ($P_{\rm ff}$) to the free-free spectral index ($\alpha_{\rm ff}$) between 3.3 cm and 1.3 mm for the sample of dust cores with an estimation of their free-free content from both a centimeter continuum and H30α detection (see Sect. 4.2). A first group of dust cores with optically thin free-free emission ($\alpha_{\rm ff} \simeq -0.1$ to 0) has $P_{\rm ff}$ spanning a large range of values from 30 to 80%. In contrast, a second group of cores with partially optically thick free-free emission ($\alpha_{\rm ff} \sim 0.3$ to 1) tends to show a more restricted $P_{\rm ff} \simeq 55$–65%, with a couple of exceptions. At first glance, HII regions are expected to smoothly evolve as they ionize and break out of their parental core (Keto 2007; Tanaka et al. 2016). During this process, they are expected to transition from denser objects with partially optically thick emission to less dense and optically thin objects (e.g., Keto et al. 2008; Galván-Madrid et al. 2009). The HMCs represent an early stage within this sequence (see Sect. 5.1). Therefore, the fact that the three HMCs within the sample of dust cores with HII emission have partially optically thick free-free emission is consistent with this scenario. Under this simple interpretation, however, the points in Fig. 7 should follow an anti-correlation, or at least the (more evolved) optically thin HII regions should have, on average, a larger $P_{\rm ff}$ than the (younger) optically thicker ones. This is not observed. Previous works on hydrodynamical simulations with ionization feedback and synthetic observations have shown that the stochastic interactions of the neutral gas and ionizing photons can

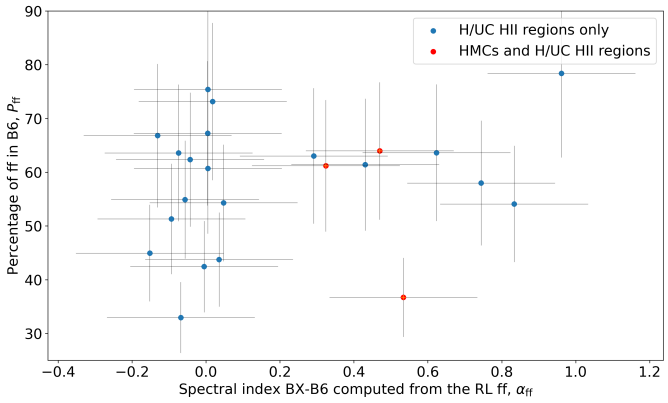

Fig. 7. Percentage of free-free emission at 1.3 mm ($P_{\rm ff}$) as a function of the spectral index of free-free emission ($\alpha_{\rm ff}$). A group of cores with a higher spectral index, $\alpha_{\rm ff} > 0.2$, can be distinguished, but $P_{\rm ff}$ and $\alpha_{\rm ff}$ are not anti-correlated. The core sample represented here is made up of 23 cores with H30α and X band detections. Cores with H/UC HII regions and HMCs are shown in red, and cores with H/UC HII regions only are shown in blue.

cause variations in the appearance of the youngest HII regions (Peters et al. 2010a), including their spectral indices (Peters et al. 2010b). This means that even if H/UC HIIs eventually break free from their cores on timescales of $\sim 10^5$ yr, their early evolution is not necessarily monotonic. We propose that this could be the cause of the observed spread of values in Fig. 7.

5.3. Lifetimes

Next, we proceed to evaluate the core lifetimes using the evolutionary sequence presented in Sect. 5.1 and shown in Fig. 5. For this purpose, we considered the population of 109 cores in W49N, which is where a more complete search of H/UC HII regions has been made. After summing up 28 cores with H/UC HII regions and 57 H/UC HII regions not associated with a dust core, 85 objects fell in the H/UC HII regions category. Under the hypothesis of constant star formation and assuming that HMCs are precursors of H/UC HII regions, the ratio of HMCs to H/UC HII regions (17/85) provides an estimation of their statistical lifetime. Using the typical lifetime for H/UC HII regions of 3×10^5 yr calculated from Galaxy-wide surveys (Churchwell 2002; Mottram et al. 2011), we estimate the lifetime of the HMC phase to be $\tau_{\rm HMC} \simeq (17/85) \cdot (3 \times 10^5) = 6 \times 10^4$ yr. The ratio of 17 HMCs to 85 H/UC HII we found in W49, and thus the inferred lifetime, are smaller than previous estimations in the same region (6/12, Wilner et al. 2001) and in Sgr B2 (5/8, Bonfand et al. 2017). However, it is similar to what was found in another high-mass star-forming region (1/9, Furuya et al. 2005). The period during which HMCs and H/UC HII regions coexist in W49A (five cores out of 17) appears to be very short, $\simeq 2 \times 10^4$ yr (see also the survey of Liu et al. 2021). Therefore, our results point toward a rapid dispersal of the warm inner molecular envelope once the HII region appears.

We also used the ratio of high-mass protostellar cores to H/UC HII regions (40/85, see Sect. 5.1) to estimate the lifetime of the massive protostellar phase, $\tau_{\rm proto} \simeq 40/85 \times 3 \times 10^5 \simeq 1.4 \times 10^5$ yr. Our estimation is about two times lower than the value reported in the review of Motte et al. (2018), $\tau_{\rm proto} \sim 3 \times 10^5$ yr. It is also within the range of durations reported by Mottram et al. (2011), 7×10^4 yr to 4×10^5 yr for massive YSOs with luminosities from 10^4 to $10^5 L_\odot$. Our estimation of the lifetime of the massive protostellar phase may be a lower limit if we are missing detections of HMCs or H/UC HII regions. For example, it has been reported that a large dust optical depth could hinder the detection of molecular lines in emission (e.g. De Simone et al. 2020). Conversely, our estimation of the number of high-mass protostars may be an upper limit if some of the HMCs are associated with intermediate-mass protostars that will not evolve to high-mass stars or if our 3000-au cores subfragment into several intermediate- and low-mass stars.

6. Conclusions

We presented an analysis of the star-formation activity in W49A based on the first millimeter continuum survey in this region. Our main results and conclusions are as follows:

1. We built a 1.3-mm continuum image at $0.29'' \times 0.24''$ resolution from ALMA B6 observations and constructed a catalog of 129 cores extracted using the *getsf* algorithm.
2. We looked for cores associated with H/UC HII regions by analyzing the VLA *X* band map (3.3 cm, De Pree et al. 2020) dominated by free-free emission and the H30α recombination line at 231.9 GHz covered by our ALMA observations. We found a good agreement between these two tracers of ionized gas, with 23 common detections and only four cores with HII regions detected only in the *X* band map, out of 109 cores within the VLA field of view.
3. We identified a total of 36 cores associated with H/UC HII regions over the entire ALMA mosaic as well as four other cores tentatively associated with H/UC HII regions. We measured their integrated free-free flux and derived their dust flux at 1.3 mm.
4. The spectral indexes from 3.3 cm to 1.3 mm range from 1, for the youngest cores with partially optically thick free-free emission, to about –0.1, which is for optically thin free-free emission obtained for cores allegedly more evolved. The emission measures, which range from 4.5×10^6 to 3.1×10^8 pc cm^{-6}, are typical of H/UC HII regions.
5. We also found, using the methyl formate doublet at 218.281 and 218.298 GHz within the spectral coverage of our ALMA B6 data, that 19 cores are associated with HMC emission. Seventeen HMCs are located within the central subregion W49N. Notably, this is about three times the number of HMCs previously reported by Wilner et al. (2001), and this finding places W49 as being among the protoclusters with the best statistics for HMC studies, along with W43 and W51(Brouillet et al. 2022; Bonfand et al. 2024).
6. We combined these two tracers of high-mass star formation (HMC and HII region emission) to propose a classification of the cores according to their evolutionary stage. Within W49N, covered by the VLA map, 69 cores without an HMC or an H/UC HII region are labeled as "young cores", meaning that they are either prestellar or lower-mass protostellar cores. The five cores with an HMC and an H/UC HII region are assumed to be more evolved than the 12 cores with only HMC.
7. We found 23 cores with an H/UC HII region and no HMC. We also included a fifth category of objects, UC HII regions not associated with dust cores. They account for two-thirds of the total number of H/UC HII regions in the considered field and represent the most evolved UC HII regions, after the dispersal of the dust envelope.
8. We estimated the statistical lifetimes of the HMC and massive protostellar phases in W49 to be 6×10^4 yr and 1.4×10^5 yr, respectively, based on the duration of the H/UC HII phase of 3×10^5 yr. The identification of massive protostellar cores is based on the association between a dust core and an HMC and/or an H/UC HII region. These estimations could be upper limits, considering the possible sub-fragmentation of HMCs into less massive protostars.
9. We found that HMCs and H/UC HII regions coexist in W49A during a short period of $\simeq 2 \times 10^4$ yr. This indicates a rapid dispersal of the inner molecule envelope once the HC HII is formed.

In summary, we conducted a comprehensive study at subarcsecond resolution of the massive protocluster W49A and provided a classification of the massive protostellar cores associated with an HMC and/or an H/UC HII region.

Acknowledgements. We thank the referee R. Miyawaki for his helpful comments improving the manuscript. R.G.M. and T.N. acknowledge support from UNAM-PAPIIT project IN108822 and from CONACyT Ciencia de Frontera project ID 86372. T.N. also acknowledges support from the postdoctoral fellowship program of the UNAM. Part of this work was performed using the high-performance computers at IRyA, Mexico, funded by CONACyT and UNAM. The work from the IT staff at this institute is acknowledged. A.G. acknowledges support from the NSF via grants AST 2008101 and CAREER 2142300. H.B.L. is supported by the National Science and Technology Council (NSTC) of Taiwan (Grant Nos. 111-2112-M-110-022-MY3). C.R.-Z. acknowledges support from program UNAM-PAPIIT IG101723. This paper makes use of the following ALMA data:

ADS/JAO.ALMA#2016.1.00620.S ALMA is a partnership of ESO (representing its member states), NSF (USA) and NINS (Japan), together with NRC (Canada), MOST and ASIAA (Taiwan), and KASI (Republic of Korea), in cooperation with the Republic of Chile. The Joint ALMA Observatory is operated by ESO, AUI/NRAO and NAOJ. This work is based on an analysis carried out with the GILDAS, IMAGER and CASSIS softwares, as well as the CDMS and JPL spectroscopic databases. CASSIS has been developed by IRAP-UPS/CNRS (http://cassis.irap.omp.eu).

References

Barnes, A. T., Kauffmann, J., Bigiel, F., et al. 2020, MNRAS, 497, 1972
Bonfand, M., Belloche, A., Menten, K. M., Garrod, R. T., & Müller, H. S. P. 2017, A&A, 604, A60
Bonfand, M., Csengeri, T., Bontemps, S., et al. 2024, A&A, in press, https://doi.org/10.1051/0004-6361/202347856
Breen, S. L., Fuller, G. A., Caswell, J. L., et al. 2015, MNRAS, 450, 4109
Brouillet, N., Despois, D., Molet, J., et al. 2022, A&A, 665, A140
CASA Team (Bean, B., et al.) 2022, PASP, 134, 114501
Churchwell, E. 2002, ARA&A, 40, 27
De Pree, C. G., Mehringer, D. M., & Goss, W. M. 1997, ApJ, 482, 307
De Pree, C. G., Wilner, D. J., Deblasio, J., Mercer, A. J., & Davis, L. E. 2005, ApJ, 624, L101
De Pree, C. G., Galván-Madrid, R., Goss, W. M., et al. 2018, ApJ, 863, L9
De Pree, C. G., Wilner, D. J., Kristensen, L. E., et al. 2020, AJ, 160, 234
De Simone, M., Ceccarelli, C., Codella, C., et al. 2020, ApJ, 896, L3
Furuya, R. S., Cesaroni, R., Takahashi, S., et al. 2005, ApJ, 624, 827
Galván-Madrid, R., Keto, E., Zhang, Q., et al. 2009, ApJ, 706, 1036
Galván-Madrid, R., Liu, H. B., Zhang, Z. Y., et al. 2013, ApJ, 779, 121
Ginsburg, A., Goss, W. M., Goddi, C., et al. 2016, A&A, 595, A27
Ginsburg, A., Csengeri, T., Galván-Madrid, R., et al. 2022, A&A, 662, A9
Gwinn, C. R., Moran, J. M., & Reid, M. J. 1992, ApJ, 393, 149
Herbst, E., & van Dishoeck, E. F. 2009, ARA&A, 47, 427
Hoare, M. G., Kurtz, S. E., Lizano, S., Keto, E., & Hofner, P. 2007, in Protostars and Planets V, eds. B. Reipurth, D. Jewitt, & K. Keil (Tucson: University of Arizona Press), 181
Homeier, N. L., & Alves, J. 2005, A&A, 430, 481
Keto, E. 2007, ApJ, 666, 976
Keto, E., Zhang, Q., & Kurtz, S. 2008, ApJ, 672, 423
Kurtz, S. 2005, IAU Symp., 227, 111
Kurtz, S., Churchwell, E., & Wood, D. O. S. 1994, ApJS, 91, 659
Lin, Y., Liu, H. B., Li, D., et al. 2016, ApJ, 828, 32
Liu, H. B., Chen, H.-R. V., Román-Zúñiga, C. G., et al. 2019, ApJ, 871, 185
Liu, H.-L., Liu, T., Evans, Neal J., I., et al. 2021, MNRAS, 505, 2801
Lizano, S. 2008, ASP Conf. Ser., 387, 232
McGrath, E. J., Goss, W. M., & De Pree, C. G. 2004, ApJS, 155, 577
Men'shchikov, A. 2021, A&A, 649, A89
Miyawaki, R., Hayashi, M., & Hasegawa, T. 2009, PASJ, 61, 39
Miyawaki, R., Hayashi, M., & Hasegawa, T. 2022a, PASJ, 74, 128
Miyawaki, R., Hayashi, M., & Hasegawa, T. 2022b, PASJ, 74, 705
Molet, J., Brouillet, N., Nony, T., et al. 2019, A&A, 626, A132
Motte, F., Bontemps, S., & Louvet, F. 2018, ARA&A, 56, 41
Mottram, J. C., Hoare, M. G., Davies, B., et al. 2011, ApJ, 730, L33
Nony, T., Galván-Madrid, R., Motte, F., et al. 2023, A&A, 674, A75
Peng, T. C., Wyrowski, F., van der Tak, F. F. S., Menten, K. M., & Walmsley, C. M. 2010, A&A, 520, A84
Peters, T., Banerjee, R., Klessen, R. S., et al. 2010a, ApJ, 711, 1017
Peters, T., Mac Low, M.-M., Banerjee, R., Klessen, R. S., & Dullemond, C. P. 2010b, ApJ, 719, 831
Pouteau, Y., Motte, F., Nony, T., et al. 2022, A&A, 664, A26
Rivera-Soto, R., Galván-Madrid, R., Ginsburg, A., & Kurtz, S. 2020, ApJ, 899, 94
Rugel, M. R., Rahner, D., Beuther, H., et al. 2019, A&A, 622, A48
Saral, G., Hora, J. L., Willis, S. E., et al. 2015, ApJ, 813, 25
Scoville, N. Z., & Kwan, J. 1976, ApJ, 206, 718
Sievers, A. W., Mezger, P. G., Bordeon, M. A., et al. 1991, A&A, 251, 231
Smith, R. J., Longmore, S., & Bonnell, I. 2009, MNRAS, 400, 1775
Tanaka, K. E. I., Tan, J. C., & Zhang, Y. 2016, ApJ, 818, 52
Vázquez-Semadeni, E., Palau, A., Ballesteros-Paredes, J., Gómez, G. C., & Zamora-Avilés, M. 2019, MNRAS, 490, 3061
Welch, W. J., Dreher, J. W., Jackson, J. M., Terebey, S., & Vogel, S. N. 1987, Science, 238, 1550
Wilner, D. J., De Pree, C. G., Welch, W. J., & Goss, W. M. 2001, ApJ, 550, L81
Wilson, T. L., Rohlfs, K., & Hüttemeister, S. 2009, Tools of Radio Astronomy (Berlin: Springer)
Zhang, B., Reid, M. J., Menten, K. M., et al. 2013, ApJ, 775, 79
Zhang, Y., Tanaka, K. E. I., Tan, J. C., et al. 2022, ApJ, 936, 68
Zhang, C., Zhu, F.-Y., Liu, T., et al. 2023, MNRAS, 520, 3245

Appendix A: Core catalog

Table A.1 lists the physical properties and detection (or non-detection) of H/UC HII regions and HMCs for the 129 cores detected at 1.3 mm in W49. The labels of H/UC HII regions previously identified at the core positions are also given.

Table A.1. Main characteristics of cores detected on the 1.3-mm continuum image.

n	R.A. Dec. [ICRS]	Region	Size [″ × ″]	*PA* [°]	$F^{\rm int}_{\rm B6}$ [mJy]	$F^{\rm int}_{\rm BX}$ [mJy]	HII	Cross ID	HMC
(1)	(2)	(3)	(4)	(5)	(6)	(7)	(8)	(9)	(10)
1	19:10:13.419 9:06:13.00	N	0.33 × 0.27	10	1031.9	36.6	BX+RL	G2a	
2	19:10:13.149 9:06:12.72	N	0.37 × 0.33	117	728.4	38.5	BX+RL	B2	
3	19:10:12.889 9:06:11.73	N	0.39 × 0.29	169	365.0	56.0	BX+RL	A2	
4	19:10:10.938 9:05:17.53	SW	0.31 × 0.27	166	94.6		RL	-	*
5	19:10:16.356 9:06:07.04	out	0.49 × 0.35	115	133.2		RL	O	
6	19:10:13.614 9:06:49.12	N	0.45 × 0.30	118	75.0	-			*
7	19:10:13.144 9:06:18.76	N	0.35 × 0.29	142	188.5	40.6	BX+RL	C	*
8	19:10:14.130 9:06:25.00	N	0.44 × 0.30	155	200.2	1.5	BX	J1	*
9	19:10:11.050 9:05:20.11	SW	0.44 × 0.40	17	85.9		RL	R	*
10	19:10:13.455 9:06:12.79	N	0.33 × 0.27	20	332.0	12.3	BX+RL	G2c	
11	19:10:15.369 9:06:14.95	N	0.40 × 0.33	174	56.2	22.0	BX+RL	N	
12	19:10:16.372 9:06:06.81	out	0.47 × 0.31	123	116.1		RL	O	
13	19:10:13.116 9:06:12.36	N	0.30 × 0.26	11	149.0	12.7	BX+RL	B1	
14	19:10:13.202 9:06:11.13	N	0.68 × 0.57	69	203.9	135.2	BX+RL	D	
15	19:10:13.340 9:06:21.37	N	0.56 × 0.47	97	59.1	60.1	BX+RL	F	
16	19:10:13.373 9:06:12.58	N	0.46 × 0.39	146	279.9	69.0	BX+RL	G1	
17	19:10:12.884 9:06:12.16	N	0.39 × 0.34	30	125.9	17.7	BX+RL	A1	*
18	19:10:13.312 9:06:19.87	N	0.44 × 0.32	172	93.3	1.0	BX	-	
19	19:10:14.645 9:06:25.97	N	0.41 × 0.40	143	20.3	-			*
20	19:10:13.279 9:06:12.79	N	0.39 × 0.29	0	82.6	-			*
22	19:10:14.628 9:06:45.96	N	0.38 × 0.33	6	10.5	-			
23	19:10:13.060 9:06:16.07	N	0.35 × 0.33	178	17.7	12.7	BX+RL	C1	
24	19:10:14.284 9:06:22.22	N	0.44 × 0.40	69	20.7	-			
25	19:10:15.358 9:06:15.36	N	0.36 × 0.33	167	21.3	-			*
26	19:10:12.665 9:06:07.57	N	0.48 × 0.44	71	25.0	-			
27	19:10:13.272 9:06:16.38	N	0.52 × 0.37	47	53.7	-			*
28	19:10:13.149 9:06:13.84	N	0.45 × 0.38	72	112.0	-			*
29	19:10:13.259 9:06:12.19	N	0.37 × 0.31	35	23.3	17.3	BX+RL	E3	
30	19:10:14.137 9:06:26.60	N	0.45 × 0.38	110	27.9	-			
31	19:10:14.312 9:06:22.21	N	0.37 × 0.27	23	11.7	-			
32	19:10:13.170 9:06:13.36	N	0.36 × 0.33	64	70.4	-			*
34	19:10:13.259 9:06:18.88	N	0.38 × 0.29	164	32.2	-			
35	19:10:13.441 9:06:07.11	N	0.28 × 0.25	27	4.5	-			
36	19:10:12.097 9:06:14.64	N	0.41 × 0.26	74	9.0	-			*
37	19:10:14.182 9:06:20.58	N	0.32 × 0.28	103	2.9	-			
39	19:10:11.671 9:05:26.86	SW	0.55 × 0.45	153	30.6		RL	S	
40	19:10:13.392 9:06:11.82	N	0.56 × 0.48	10	79.0	54.8	BX+RL	G1S	
42	19:10:14.664 9:06:25.53	N	0.45 × 0.36	107	12.0	-			
43	19:10:13.348 9:06:16.05	N	0.39 × 0.33	155	25.9	-			*
44	19:10:12.703 9:06:11.29	N	0.31 × 0.26	24	22.2	1.5	BX+RL	-	*
45	19:10:13.211 9:06:14.30	N	0.31 × 0.27	26	24.8	-			
46	19:10:13.498 9:06:11.77	N	0.36 × 0.32	179	58.1	34.7	BX+RL	G3b	
47	19:10:13.498 9:06:12.42	N	0.37 × 0.26	8	43.7	20.3	BX+RL	G3a	
48	19:10:13.721 9:06:44.58	N	0.37 × 0.33	53	3.6	-			
49	19:10:12.671 9:06:18.28	N	0.39 × 0.29	172	7.0	-			

(1) Core number in the getsf catalog. (2) Right ascension and declination coordinates. (3) Subregion: (W49-)N, (W49-)SW, or (W49)-out(skirts). (4) FWHM major and minor axis. (5) Position angle (west to north) of the ellipse. (6,7) Integrated fluxes in B6 and BX. (8) Detection of the H/UC HII region in X band 3.3 cm (BX) and/or in H30α (RL). (9) Identification of the associated H/UC HII region in the catalogs of De Pree et al. (1997, 2020). (10) Cores associated with a HMC emission are marked with an asterisk (*).

Table A.1. Continued.

n	R.A. Dec. [ICRS]	Region	Size [″ × ″]	*PA* [°]	$F^{\rm int}_{\rm B6}$ [mJy]	$F^{\rm int}_{\rm BX}$ [mJy]	HII	Cross ID	HMC
(1)	(2)	(3)	(4)	(5)	(6)	(7)	(8)	(9)	(10)
50	19:10:10.686 9:05:16.78	SW	0.95 × 0.70	134	36.7		RL	R3	
51	19:10:12.644 9:06:18.93	N	0.39 × 0.30	37	4.0	-			
52	19:10:16.504 9:06:04.24	out	0.63 × 0.53	23	11.4				
53	19:10:13.364 9:06:18.01	N	0.44 × 0.41	88	10.3	-			
54	19:10:13.323 9:06:16.32	N	0.33 × 0.30	27	16.8	-			*
55	19:10:13.230 9:06:54.16	N	0.72 × 0.58	130	4.1	-			
56	19:10:13.188 9:06:12.85	N	0.45 × 0.36	0	81.5	-			*
57	19:10:13.114 9:06:13.77	N	0.42 × 0.37	120	62.3	-			
58	19:10:16.666 9:05:49.88	out	0.44 × 0.32	53	7.2				
59	19:10:16.402 9:06:07.36	out	0.47 × 0.36	143	22.8		RL	-	
60	19:10:15.754 9:06:05.78	N	0.49 × 0.40	169	4.7	-			
61	19:10:15.256 9:06:10.99	N	0.32 × 0.29	92	2.1	-			
62	19:10:12.843 9:06:11.44	N	0.61 × 0.42	149	76.7	-			
63	19:10:14.605 9:06:26.38	N	0.45 × 0.32	4	7.2	-			
65	19:10:14.159 9:06:21.56	N	0.60 × 0.54	110	14.2	-			
66	19:10:13.385 9:06:19.37	N	0.40 × 0.36	37	19.7	-			
67	19:10:13.656 9:06:21.49	N	0.57 × 0.43	46	10.0	-			
68	19:10:12.800 9:06:27.54	N	0.54 × 0.34	85	6.9	-			
69	19:10:14.186 9:06:15.32	N	0.66 × 0.41	42	21.3	17.2	BX+RL	J	
70	19:10:12.746 9:06:10.33	N	0.36 × 0.32	53	24.0	-			
71	19:10:13.434 9:06:22.78	N	0.46 × 0.36	155	7.1	-			
72	19:10:13.178 9:06:18.28	N	0.50 × 0.40	143	42.5	31.2	BX+RL	C	
73	19:10:13.601 9:06:11.02	N	0.43 × 0.30	0	45.6	30.1	BX+RL	G3d	
74	19:10:14.563 9:06:20.47	N	0.50 × 0.40	50	8.7	3.6	BX+RL	L	
75	19:10:14.126 9:06:24.28	N	0.33 × 0.21	20	17.8	-			
76	19:10:13.323 9:06:25.53	N	0.47 × 0.31	124	6.0	-			
77	19:10:13.898 9:06:36.91	N	0.29 × 0.24	47	1.5	-			
78	19:10:16.344 9:06:07.75	out	0.53 × 0.49	111	21.8		RL	-	
79	19:10:13.018 9:06:17.05	N	0.60 × 0.55	90	16.2	-			
80	19:10:10.801 9:05:19.45	SW	1.03 × 0.77	137	25.9				
81	19:10:14.610 9:06:02.65	N	0.47 × 0.37	41	6.0	-			
82	19:10:14.178 9:06:26.65	N	0.34 × 0.29	55	9.1	-			
83	19:10:13.135 9:06:13.45	N	0.43 × 0.38	75	83.7	-			
84	19:10:12.329 9:06:18.58	N	0.28 × 0.25	176	2.0	-			
85	19:10:12.720 9:06:28.69	N	0.30 × 0.28	18	2.8	-			
86	19:10:13.234 9:06:12.68	N	0.44 × 0.40	177	49.8	-			
87	19:10:14.184 9:06:14.37	N	1.05 × 0.94	178	32.2	13.9	BX+RL	J	
88	19:10:12.613 9:06:22.60	N	0.43 × 0.31	168	3.5	-			
89	19:10:13.231 9:06:08.87	N	0.53 × 0.38	152	9.6	-			
90	19:10:15.433 9:06:16.78	N	0.43 × 0.32	11	3.3	-			
91	19:10:11.174 9:05:53.85	N	0.45 × 0.34	12	3.1	-			
92	19:10:12.685 9:06:32.36	N	0.97 × 0.90	127	7.3	-			
93	19:10:15.317 9:06:14.80	N	0.54 × 0.34	5	13.4	-			
94	19:10:14.509 9:06:22.47	N	1.06 × 0.82	67	25.7	-	RL	L	
95	19:10:11.487 9:05:32.14	N	0.31 × 0.27	24	2.4	-			
96	19:10:13.571 9:06:21.34	N	0.47 × 0.35	173	9.9	-			
97	19:10:13.307 9:06:17.02	N	0.37 × 0.29	162	15.2	-			
98	19:10:14.796 9:06:44.25	N	0.68 × 0.47	81	5.8	-			
99	19:10:15.807 9:06:05.59	N	0.29 × 0.27	157	1.4	-			
100	19:10:11.490 9:06:24.34	N	0.35 × 0.29	11	1.5	-			
101	19:10:13.459 9:06:20.14	N	0.49 × 0.32	144	15.4	-			
102	19:10:12.779 9:06:11.13	N	0.34 × 0.29	24	19.5	-			
103	19:10:14.825 9:06:36.88	N	0.69 × 0.50	140	5.1	-			
104	19:10:14.037 9:06:23.56	N	0.41 × 0.35	122	15.5	0.7	BX	-	*
105	19:10:13.630 9:06:20.30	N	1.03 × 0.86	146	33.5	-			

Notes. (1) Core number in the getsf catalog. (2) Right ascension and declination coordinates. (3) Subregion: (W49-)N, (W49-)SW, or (W49)-out(skirts). (4) FWHM major and minor axis. (5) Position angle (west to north) of the ellipse. (6,7) Integrated fluxes in B6 and BX. (8) Detection of the H/UC HII region in X band 3.3 cm (BX) and/or in H30α (RL). (9) Identification of the associated H/UC HII region in the catalogs of De Pree et al. (1997, 2020). (10) Cores associated with a HMC emission are marked with an asterisk (*).

Table A.1. Continued.

n	R.A. Dec. [ICRS]	Region	Size [″ × ″]	*PA* [°]	$F^{\rm int}_{\rm B6}$ [mJy]	$F^{\rm int}_{\rm BX}$ [mJy]	HII	Cross ID	HMC
(1)	(2)	(3)	(4)	(5)	(6)	(7)	(8)	(9)	(10)
106	19:10:12.720 9:06:28.38	N	0.41 × 0.39	52	4.5	-			
107	19:10:16.297 9:06:06.66	out	0.55 × 0.40	157	14.8		RL	-	
108	19:10:13.719 9:06:25.03	N	0.40 × 0.34	111	5.1	-			
109	19:10:14.237 9:06:28.51	N	0.48 × 0.37	162	11.0	-			
110	19:10:15.409 9:06:11.87	N	0.65 × 0.36	2	5.8	-			
111	19:10:11.629 9:06:16.03	N	0.35 × 0.26	172	3.4	-			
112	19:10:11.731 9:05:27.37	SW	0.67 × 0.43	10	25.7		RL	S	
113	19:10:10.277 9:05:14.07	SW	0.30 × 0.23	160	4.5				
114	19:10:12.838 9:06:29.46	N	0.34 × 0.27	180	3.0	-			
115	19:10:16.826 9:05:49.99	out	0.83 × 0.66	4	11.1				
116	19:10:14.747 9:06:25.65	N	0.50 × 0.34	150	4.9	3.4	BX+RL	M	
117	19:10:13.683 9:06:10.06	N	0.36 × 0.34	119	6.4	2.4	BX	-	
119	19:10:10.956 9:05:18.60	SW	0.34 × 0.25	90	2.5				
120	19:10:14.284 9:06:32.28	N	0.55 × 0.53	52	11.3	-			
121	19:10:14.253 9:06:29.98	N	0.42 × 0.35	115	4.0	-			
122	19:10:12.416 9:06:06.76	N	0.75 × 0.64	72	8.4	-			
123	19:10:10.758 9:05:21.46	SW	0.30 × 0.23	34	1.7				
124	19:10:13.735 9:06:49.42	N	0.44 × 0.40	147	4.4	-			
125	19:10:14.685 9:06:45.97	N	0.33 × 0.24	12	2.4	-			
126	19:10:13.779 9:06:16.81	N	0.38 × 0.26	15	3.5	-			
128	19:10:16.708 9:05:49.17	out	0.34 × 0.27	73	3.4				
130	19:10:13.780 9:06:22.11	N	0.37 × 0.29	173	4.1	-			
131	19:10:10.541 9:05:14.08	SW	0.30 × 0.25	124	3.2		RL	Q	
133	19:10:14.122 9:06:26.01	N	0.39 × 0.35	65	9.9	-			*
138	19:10:14.525 9:06:28.78	N	0.40 × 0.30	173	1.7	-			
140	19:10:14.262 9:06:26.22	N	0.36 × 0.26	117	3.0	-			
141	19:10:13.980 9:06:24.90	N	0.34 × 0.27	103	2.9	-			
142	19:10:14.980 9:06:03.82	N	0.30 × 0.23	142	1.7	-			
147	19:10:10.893 9:05:16.78	SW	0.95 × 0.68	152	20.0		RL	-	